

OrbitGrasp: SE(3)-Equivariant Grasp Learning

Boce Hu¹, Xupeng Zhu^{*1}, Dian Wang^{*1}, Zihao Dong^{*1}, Haojie Huang^{*1},
Chenghao Wang^{*1}, Robin Walters¹, Robert Platt^{1,2}

* Equal Contribution

¹Northeastern University

²Boston Dynamics AI Institute

{hu.boce; r.walters; r.platt}@northeastern.edu

Abstract: While grasp detection is an important part of any robotic manipulation pipeline, reliable and accurate grasp detection in SE(3) remains a research challenge. Many robotics applications in unstructured environments such as the home or warehouse would benefit a lot from better grasp performance. This paper proposes a novel framework for detecting SE(3) grasp poses based on point cloud input. Our main contribution is to propose an SE(3)-equivariant model that maps each point in the cloud to a continuous grasp quality function over the 2-sphere S^2 using a spherical harmonic basis. Compared with reasoning about a finite set of samples, this formulation improves the accuracy and efficiency of our model when a large number of samples would otherwise be needed. In order to accomplish this, we propose a novel variation on EquiFormerV2 that leverages a UNet-style backbone to enlarge the number of points the model can handle. Our resulting method, which we name *OrbitGrasp*, significantly outperforms baselines in both simulation and physical experiments.

Keywords: Grasp Detection, Equivariance, Symmetry, Grasp Learning

1 Introduction

The ability to detect and evaluate good grasp poses in a manipulation scene is a critical part of robotic manipulation. Despite extensive recent work in the area, e.g. [1, 2, 3, 4, 5, 6, 7, 8, 9], grasp detection is still not accurate and reliable enough for many practical applications. A key challenge here is effective reasoning over hand poses in SO(3), i.e. the three dimensions of orientation spanned by SE(3). Simply representing orientations in SO(3) can be a challenge due to classic problems like gimble lock [10] and discontinuity [11]. More importantly, it would be very helpful to be able to infer grasp quality over a continuous range of orientations in SO(3) – something which is a major challenge for conventional grasp methods. Finally, since SE(3) grasping problems are often equivariant (i.e. symmetric) in SO(3), it is often desirable to encode symmetry assumptions into the model.

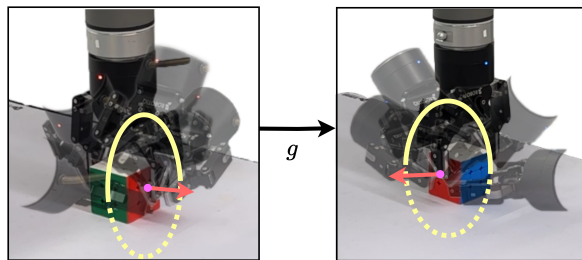


Figure 1. We reason about an orbit of grasps (yellow ellipse) defined relative to the surface normal (red arrow) at a contact point (pink dot). Since our model is equivariant over SO(3), the optimal pose on the orbit rotates when the scene rotates (left and right show a rotation by 90 degrees).

This paper addresses these challenges by leveraging recent innovations in equivariant point models [12, 13, 14, 15]. Specifically, we use a model that maps each point in a point cloud to a grasp quality function over the 2-sphere S^2 . For each point in the cloud, this function encodes grasp quality for the space of possible hand approach directions toward that point. An important question here is how to represent this quality function over S^2 . Following recent work [1, 16, 8], our approach is

to leverage the spherical harmonic basis. Specifically, at each point in the cloud, the neural network outputs a vector of Fourier coefficients to the spherical harmonic basis functions, thereby defining a grasp quality function over hand approach directions. With this learned per-point grasp distribution, we can evaluate the quality of a large number of potential grasp poses quickly and easily, thereby more easily locating a grasp appropriate for a given downstream manipulation task.

To summarize, this paper makes a few key contributions. First, we propose a novel method of using spherical harmonics to reason about an *orbit* (i.e. a S^1 manifold embedded in S^2) of grasp approach directions defined relative to the surface normal at each contact point in the point cloud, as shown in Figure.1. Second, we propose a modification of a recently developed SE(3)-equivariant model known as EquiFormerV2 [17], incorporating a U-Net backbone and thereby enabling the model to accommodate a larger number of points in the point cloud. Finally, we evaluate our method against multiple baselines drawn from the literature [5, 18, 8, 9] using the *Packed* and *Piled* benchmark tasks proposed in [5]. The results indicate that our approach, which we name *OrbitGrasp*, convincingly outperforms the baselines in both the single-view and multi-view settings, both in the simulation and in physical experiments.

2 Related Work

SE(3) Grasp Detection: Current 6-DoF grasping tasks in cluttered tabletop scenarios primarily use a volumetric-based or point cloud-based scene representation as input and output one or more optimal grasp poses [7, 3, 19, 2]. Volumetric Grasping Network (VGN) [5] and Grasp detection via Implicit Geometry and Affordance (GIGA) [18] use 3D convolutional models to reason about a 3D truncated signed distance function (TSDF). However, these methods suffer from high memory consumption and resolution limitations. In contrast, point clouds can provide higher resolution, but they are more difficult to reason about because they are less structured. One approach to adding structure is to leverage equivariant point cloud models [20, 21]. For example, EdgeGrasp [8] introduced a method based on a vector neuron model that evaluates the quality of a set of finite grasp candidates defined by associating each point in the cloud with a finite set of candidates. CAPGrasp [22] is another equivariant model that samples grasp candidates while constraining the gripper approach direction to be within a certain angular distance of the surface normal at the associated point. Other recent grasping methods leverage surface reconstruction of the object to be grasped. For example, NeuGraspNet [23] defines grasping as a surface rendering task and sample grasp candidates using global rendering, and ICGNet [9] is an instance-centric-based grasping method that reconstructs the scene during the grasping process.

Equivariance in Robot Learning: Using symmetry, i.e. equivariance, in robot learning tasks has recently been used to improve sample efficiency and generalization. The work of [24, 25] introduces equivariant neural network models in the form of steerable convolutional layers [26, 27] to SE(2) manipulation tasks. [28] applies similar models to transporter network [29], making it bi-equivariant and significantly improving sample efficiency. EDF [30] introduces an equivariant energy model that produces a continuous distribution over pose. Fourtran [31] extends [28] from SE(2) to SE(3) using a Fourier representation of rotations. [32] develops a novel, dense, interpretable representation for relative object placement tasks. RiEMann [33] presents the first near real-time SE(3)-equivariant robot manipulation framework for point cloud inputs, addressing problems related to slow inference over the SE(3)-manifold. Most relevant to this paper is [1] who are the first to apply steerable convolutional layers to create an SE(2)-equivariant grasp model that is sample efficient enough to learn a good grasp function using only physical robotic experiences. Also relevant is [8], who introduce an SE(3)-invariant grasping method based on vector neurons.

OrbitGrasp: The method proposed in this paper, *OrbitGrasp*, is distinct from the work described above in a couple of important ways. First, prior work in grasp detection is generally sample-based [34, 7, 6], i.e., they evaluate grasp quality for a (large) finite set of samples or discrete voxel/pixel locations. In contrast, *OrbitGrasp* evaluates grasp quality for a *continuous* range of approach directions by inferring the parameters of spherical harmonic basis functions over S^2 . This is simultaneously

more computationally efficient and more precise than sample-based methods. Another distinction between OrbitGrasp and prior work is that the representation of rotation in terms of high degrees of spherical harmonics encodes continuous equivariant constraints more accurately and, therefore, models the grasp function better.

3 Background

We introduce concepts from group theory and SE(3)-equivariant neural networks, which are key to our method. For additional background, see, e.g., [35].

Representations of SE(3): Our work focuses on the special Euclidean group $SE(3) = SO(3) \times \mathbb{R}^3$ of 3D rotations and translations. A representation of a group G is a homomorphism $\rho: G \rightarrow GL(V)$ mapping each group element g to an invertible linear operator on the vector space V . The representation (ρ, V) is an irreducible representation, or irrep, if no non-trivial subspace $W \subset V$ is closed under the action of G . The irreps of $SO(3)$ are classified by positive integers $l \in \mathbb{Z}_{\geq 0}$ with the irrep V_l of type l having dimension $2l + 1$. For example, $l = 1$ gives the standard rotation action on \mathbb{R}^3 . The group action on V_l is given by the Wigner D-matrices $D^l: SO(3) \rightarrow GL(V_l)$ of size $(2l + 1) \times (2l + 1)$. Traditionally, the Wigner D-matrices are parameterized by Euler angles (α, β, γ) and indexed symmetrically about 0 as $D^l_{m'm}(\alpha, \beta, \gamma)$ where $-l \leq m, m' \leq l$.

Spherical Harmonics: The real spherical harmonics (SH) are functions on the sphere $Y_l^m: S^2 \rightarrow \mathbb{R}$ indexed by $l \in \mathbb{Z}_{\geq 0}$ and $-l \leq m \leq l$. As a set they define an orthonormal basis of the Hilbert space of square-integrable functions on the sphere $L^2_{\mathbb{R}}(S^2) = \{f: S^2 \rightarrow \mathbb{R} : \int_{S^2} |f|^2 < \infty\}$. That is, given $f: S^2 \rightarrow \mathbb{R}$, we can write $f(\theta, \phi) = \sum_{l=0}^{\infty} \sum_{m=-l}^l \mathcal{F}_l^m Y_l^m(\theta, \phi)$ where \mathcal{F}_l^m are the Fourier coefficients of f . The mapping FT: $f \mapsto \{\mathcal{F}_l^m\}$ is known as the spherical Fourier transform. Approximating f by storing the \mathcal{F}_l^m up to degree $l \leq L$ gives an efficient way to encode the spherical signal f . The spherical harmonics are compatible with the $SO(3)$ action on the sphere, making them suitable for use in $SO(3)$ -equivariant networks. The rotation of a spherical signal f can be computed in Fourier space using Wigner D-matrices. Let $g \in SO(3)$. Define $f' = g \cdot f$ to be the rotated spherical signal defined $(g \cdot f)(u) = f(g^{-1} \cdot u)$ for $u \in S^2$. Denote the Fourier coefficients of f' by $\text{FT}(f') = \{\mathcal{F}_l^{m'}\}$. Then in terms of the Fourier coefficients of f we have $\mathcal{F}_l^{m'} = D^l(g) \mathcal{F}_l^m$ where \mathcal{F}_l denotes the vector $\mathcal{F}_l = (\mathcal{F}_l^m)_{m=-l}^l$.

EquiFormerV2: EquiFormerV2 [17] is a SE(3)-Equivariant Graph Neural Network (GNN) that addresses the high computational costs and poor generalization of higher-degree irreps in EquiFormer [36]. It accomplishes this by integrating eSCN [37], which uses $SO(2)$ linear operations for efficient tensor products, allowing it to capture higher frequency information with higher degree representations. Unfortunately, since EquiFormer and EquiFormerV2 were developed for applications in computational biology, they have a hard time scaling to point cloud data, which generally contain more points than molecules do atoms. To address this limitation, our paper proposes a variation of EquiFormerV2 that uses a U-Net model to handle the larger number of points. Compared to [38], our new model can reason about higher-degree spherical harmonic functions.

4 Method

4.1 Problem Statement

Given a point cloud $\mathcal{P} \subset \mathbb{R}^3$ captured by one or multiple depth cameras, our objective is to identify a set of good grasp poses. Specifically, we want to estimate a function $\Gamma: (\mathcal{P}, a) \mapsto [0, 1]$ which maps the point cloud \mathcal{P} and the hand pose $a \in SE(3)$ to the probability of successful grasp. Notice that we expect Γ to be invariant to translations and rotations $g \in SE(3)$, i.e. we expect $\Gamma(g \cdot \mathcal{P}, g \cdot a) = \Gamma(\mathcal{P}, a)$. This reflects an assumption that the probability that a grasp is successful does not change when both the scene and the grasp pose transform in concert.

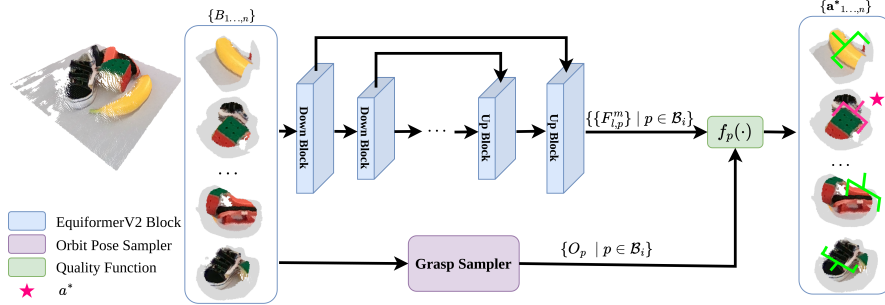


Figure 2. OrbitGrasp takes the point cloud B_i (a neighborhood about center point c_i) as input and outputs a grasp distribution for each point with grasp quality, represented as a vector of Fourier coefficients, $\mathcal{F}_{l,p}^m$. We evaluate this distribution of all points and select the grasp with the maximum quality, thereby generating the grasp poses a^* shown at right.

4.2 Summary of Approach

Figure 2 illustrates our model and approach. First, we downsample and crop the point cloud into a small number of point neighborhoods B_1, \dots, B_k . Then, we evaluate our model for each B_i . For each point $p \in B_i$, the model predicts the grasp quality over the space of possible hand approach directions, represented as a function f_p over S^2 . We densely sample this function over an *orbit* of approach directions orthogonal to the object surface normal and obtain a single grasp that maximizes quality over the orbit at p . The result is a single-hand orientation in $SO(3)$ at each point in the cloud, corresponding to a good grasp. This produces a dense sampling of grasps that can be filtered further for downstream tasks. This approach has a few important advantages. First, since our model outputs a *continuous* distribution over S^2 , it generalizes better over orientation than would a sample-based approach. Second, since our model is $SE(3)$ -equivariant, it incorporates problem symmetry as an inductive bias into the model. Finally, the approach only considers grasps that make contact parallel to the object surface normal, thereby incorporating an additional geometric prior.

4.3 Sampling k Center Points

We prepare the point cloud for processing by the prediction model as follows. First, we downsample the input point cloud \mathcal{P} to a tractable number of points $\bar{\mathcal{P}}$ (around 4k to 6k). Rather than passing the entire point cloud through our model (which would be expensive), we define smaller point clouds $B_1, \dots, B_k \subset \bar{\mathcal{P}}$ which we evaluate over separately (k is usually around 10). The B_i are defined as neighborhoods of k center points c_1, \dots, c_k from $\bar{\mathcal{P}}$ selected as follows. If a segmentation of the point cloud into objects is available, then these k center points could be the 3D positions of the centers of individual object masks. Otherwise, these centers could be random samples obtained using farthest point sampling (FPS). In our experiments, we generated the center points using object masks for training and FPS for inference. A detailed description of our mask-based sample generation is provided in Appendix A. We then construct each B_i as a neighborhood around c_i as follows. First denote the set of points contained within radius r_l ball centered at c_i by $B_i = \mathcal{B}(c_i, r_l) = \{p \in \bar{\mathcal{P}} \mid \|p - c_i\| \leq r_l\}$ for a parameterized radius r_l . Since the grasp quality at a point p depends on the geometry of a sufficiently large neighborhood of p to avoid boundary effect, we then set $B_i = \mathcal{N}(c_i, m)$ to be the m nearest neighbors of c_i , where m is chosen large enough such that $\mathcal{B}_i \subset B_i$ and B_i is larger by a fair margin. The larger point cloud B_i is passed as input to the model, but the output grasp quality is only inferred over the smaller point cloud \mathcal{B}_i . This assures inference is only performed on points with sufficient geometric context.

4.4 Representing Grasp Quality Over S^2

We model the grasp quality function $\Gamma: (\mathcal{P}, a) \mapsto [0, 1]$ with a neural network $\bar{\Gamma}: B_i \mapsto \{f_p: S^2 \rightarrow \mathbb{R} \mid p \in B_i\}$ that takes each of the k neighborhoods B_1, \dots, B_k in $\bar{\mathcal{P}}$ as input. For each B_i , the model outputs a spherical function $f_p: S^2 \rightarrow \mathbb{R}$ for each $p \in B_i$. The function f_p

represents the grasp quality over all approach directions in S^2 at the point p . The function f_p is represented by Fourier coefficients of the spherical harmonics,

$$f_p(\theta, \phi) = \sum_{l=0}^n \sum_{m=-l}^l \mathcal{F}_{l,p}^m Y_l^m(\theta, \phi). \quad (1)$$

where $Y_l^m(\theta, \phi)$ denotes the spherical harmonic of degree l and order m evaluated at the point on S^2 defined in spherical coordinates (θ, ϕ) . Concretely, the model outputs the set of Fourier coefficients $\{\mathcal{F}_{l,p}^m\}$ for each $p \in B_i$.

4.5 Implementing $\bar{\Gamma}$ as an Equivariant Neural Network

We implement $\bar{\Gamma}$ using a modified version of EquiFormerV2 [17], a fully SE(3)-equivariant, GNN-based network designed for handling node-based data. In the original EquiFormerV2 [17], all nodes are fully connected. However, in order to handle the larger number of points in our point clouds, we developed a UNet-based version of the model, which has a greater capacity (inspired by [38]). Figure 2 illustrates the model architecture. Given the point cloud B_i , successive blocks in our model sequentially downsample the points using FPS. As the number of points decreases, the radius of the edge in the graph increases, allowing distant points to communicate, expanding the receptive field per block, and capturing global features. To recover the features of each point in the original point cloud after downsampling, we upsample point features back by inverting the edges: during downsampling, we record the source and target edges in each block, and during upsampling, we swap these edges. This ensures that features gathered during downsampling are effectively propagated back to the original points. In addition, we employ skip connections between each downsample block and its corresponding upsample block to aggregate features and prevent degradation. Details of the architecture are in Appendix B. This model satisfies the desired SE(3) equivariance constraint described in Section 4.1, $\bar{\Gamma}(gB_i) = g\bar{\Gamma}(B_i) = \{g \cdot f_p : S^2 \rightarrow \mathbb{R} \mid p \in gB_i\}$. For $g \in \text{SO}(3)$, if the input point cloud is rotated gB_i , the equivariance constraints ensure the output Fourier coefficients are also transformed $D^l(g)\mathcal{F}_{l,p}$. Evaluating at a transformed grasp $g \cdot u$ thus gives the same quality of a successful grasp $(g \cdot f_p)(g \cdot u) = f_p(g^{-1} \cdot g \cdot u) = f_p(u)$.

4.6 Inferring Grasp Pose

Since our neural network model only infers grasp quality over S^2 , we constrain the remaining DoFs of the grasp pose in SE(3) by leveraging the geometric constraints of an antipodal grasp. First, for each region B_i and point $p \in B_i \subset B_i$, we constrain the contact point of the grasp to be p . Second, we constrain the hand y -axis to be the direction of the surface normal n_p of the object at $p \in B_i$ (see Figure 3), estimated using standard methods, e.g., an eigendecomposition of the covariance matrix of the points nearby p . Under these two constraints, there is only *one* degree of freedom remaining. That is, three position dimensions and two orientation dimensions have been fixed. The valid orientations form a submanifold in $\text{SO}(3)$ homeomorphic to a 1-sphere S^1 which we call the *orbit at p*

$$O_p = \{R = [r_1, n_p, r_3] \in \text{SO}(3)\} \quad (2)$$

where r_1, n_p, r_3 are the columns of the 3-by-3 rotation matrix R . Valid orientations are determined by the z -axis of the gripper (the approach direction of the hand) which may be any unit vector perpendicular to n_p . We may thus specify valid grasps by their approach vector $r_3 \in \bar{O}_p = \{r_3 \in S^1 : n_p^\top r_3 = 0\}$ since $r_1 = -n_p \times r_3$. The spherical signal f_p , which the model outputs, thus refers to grasp orientations by their approach vector r_3 . Notice that the unit vector r_3 is a direction and can be represented by spherical coordinates (θ, ϕ) . While f_p may hypothetically be evaluated at any $u \in S^2$, in practice during training and inference, we only evaluate at $u \in \bar{O}_p$. Using Equation 1,

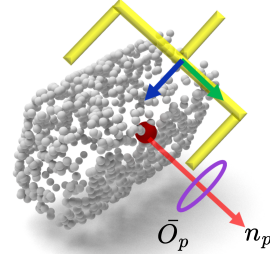


Figure 3. Green and blue denote the y, z directions of the hand, and n_p is the normal vector at p (red). Purple is the orbit of the approach direction.

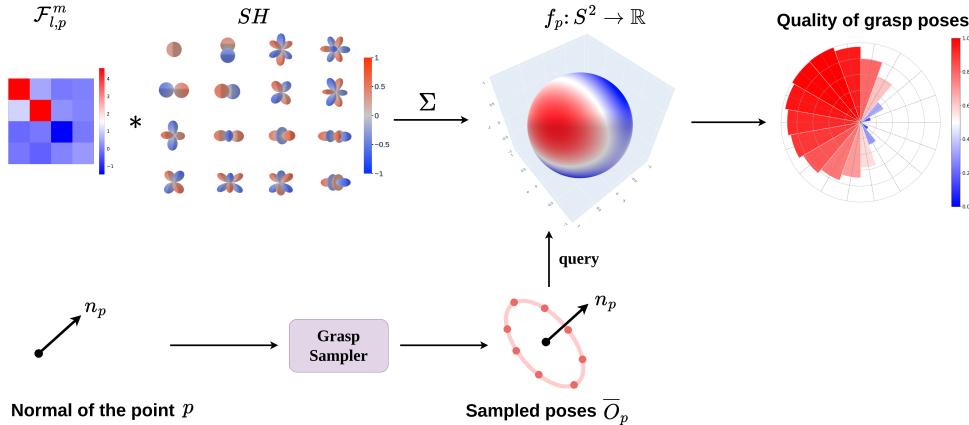


Figure 4. **Visualization of grasp poses sampling and evaluation.** To enhance clarity, this procedure is illustrated using one point p in the point cloud. The Fourier coefficients of p , denoted as $\mathcal{F}_{l,p}^m$, and the spherical harmonics basis functions SH are used to reconstruct the grasp quality function $f_p: S^2 \rightarrow \mathbb{R}$ on the 2-sphere S^2 , as detailed in Equation 1. The circle on the top right, viewed along the normal direction of point p , shows the grasp quality of each sampled pose, with redder colors indicating higher quality.

we evaluate f_p over \bar{O}_p and select the pose that maximizes f_p . This maximization is achieved by densely sampling \bar{O}_p .

Figure 4 visualizes the procedure for evaluating grasp poses on the *orbit* of point p in the point cloud. Given the point normal vector n_p and the Fourier coefficients $\mathcal{F}_{l,p}^m$ output from the network, the spherical harmonics basis function is first multiplied with the coefficients to reconstruct the spherical harmonics signals on S^2 , corresponding to Equation 1. These signals can be used as the grasp quality function, i.e., $f_p: S^2 \rightarrow \mathbb{R}$. The orbit grasp sampler then takes the normal vector as input and outputs a set of approach vectors $\{r_3 \in \bar{O}_p = \{r_3 \in S^1 : n_p^\top r_3 = 0\}\}$. These vectors are used to query f_p by Equation 1 to yield the grasp quality of each approach vector and ultimately generate the optimal pose candidate.

5 Experiments

Simulation Environment: We evaluated our model in simulation using PyBullet [39]. Our setting is the same as that used in [18, 5, 8, 9]. The workspace size is a 30 cm^3 cube and contains varying numbers of objects randomly placed within it. The object dataset includes 303 training and 40 test objects from [40, 41, 42, 43]. A Franka-Emika Panda floating gripper is used to grasp objects in the workspace. We evaluated two camera configurations. The first is a single-view setting where a camera is positioned randomly on a spherical region around the workspace. The second is a three-camera multi-view setting. Following [5], we evaluate two different grasping tasks: a *Pile* setting where objects are randomly dropped into the workspace and a *Packed* setting where objects are placed upright in random poses. See more details in Appendix C.

Generating Training Data: We generate data in simulation in both single-view and multi-view settings. A random number of objects are loaded into the workspace. Then, one or multiple depth cameras capture the scene, retaining the point clouds in the workspace. We add Gaussian noise sampled from $N(0, 0.001)$ to the point cloud to simulate real-world scenarios. After creating the scenes, we must generate training data for the grasp model. First, we obtain object masks using the Segment Anything Model (SAM) [44]. For each masked object, we randomly select a set of candidate grasp points. Then, for each point, we evaluate a set of 36 candidate grasp orientations that satisfy Equation 2, i.e. where the gripper z axis is orthogonal to the object surface normal at contact. In total, we generate approximately 6M grasp poses for each camera setting: 4M from 2,500 *Pile* scenes and 2M from 800 *Packed* scenes. The data is split with 90% used for training and 10% for validation. More details on the segmentation process can be found in Appendix A.

Setting	Method	Packed		Pile	
		GSR (%)	DR (%)	GSR (%)	DR (%)
Single-view	GIGA [18]	89.9 ± 1.7	87.6 ± 2.0	76.3 ± 2.4	80.9 ± 4.1
	GIGA-HR [18]	91.4 ± 1.5	88.5 ± 1.4	86.5 ± 1.2	80.8 ± 1.9
	EdgeGrasp [8]	92.5 ± 0.9	94.3 ± 1.1	91.5 ± 1.3	92.5 ± 1.3
	VNEdgeGrasp [8]	91.6 ± 1.7	94.4 ± 1.5	92.0 ± 1.8	92.2 ± 2.1
	ICGNet [9]	97.7 ± 0.9	97.5 ± 0.3	92.0 ± 2.6	94.1 ± 1.4
	OrbitGrasp (Ours)	98.3 ± 0.7	98.8 ± 0.6	96.7 ± 1.1	97.9 ± 0.5
Multi-view	VGN [5]	89.8 ± 2.0	82.6 ± 3.2	63.2 ± 1.1	45.6 ± 0.7
	VNEdgeGrasp [8]	97.1 ± 1.3	96.1 ± 0.5	95.1 ± 1.0	95.5 ± 1.5
	OrbitGrasp (Ours)	99.0 ± 0.6	99.2 ± 0.3	98.5 ± 0.6	98.2 ± 0.6

Table 1. We compared the results of OrbitGrasp with various baselines using the same metrics as [8]. For the single-view setting, we tested pretrained models from [8] and obtained results for GIGA, GIGA-HR, and ICGNet directly from [9]. For the multi-view setting, we retrained VNEdgeGrasp and tested the pretrained VGN model for comparison. Best results are marked with **bold** and second best results underlined.

Training Details: Since our training data is segmented into objects, we use the center of every mask as the center point c_i and obtain the local point neighborhood B_i . We train our model with the AdamW optimizer[45], starting with a learning rate of 1e-4 and using a cosine annealing scheduler [46]. We apply binary cross-entropy loss for each grasp pose and a dropout rate [47] of 0.1 to prevent overfitting. Our network is trained for 20 epochs, taking approximately 30 hours on 22k point clouds. Each SGD step takes 0.25 seconds with a batch size of 1. The model is trained on an NVIDIA RTX 4090 GPU.

5.1 Comparison With Baseline Methods in Simulation

Baselines: We compare our method with several strong baselines. In the single random view setting, we compare it with volumetric-based methods: GIGA and GIGA-HR (high resolution) [18]. Since GIGA was trained under a fixed view, we compare it with the results from [9], which retrains it under a random view setting. We also compare our method with EdgeGrasp and VNEdgeGrasp [8], two point cloud-based methods, where VNEdgeGrasp is SE(3)-invariant. Finally, we compare our method with ICGNet [9], an approach focused on partial observation to object-centric grasping that reconstructs the full 3D shape of objects before finding grasps. In the multi-view setting, we compare our method with VGN [5], which takes a TSDF as input and generates a single grasp pose per voxel, as well as VNEdgeGrasp [8] trained in the multi-view setting.

Results: We report the comparison result in Table.1 under two different settings, single-view and multi-view, and two different tasks, *Packed* and *Pile*. Performance is evaluated based on two metrics: (1) Grasp Success Rate (GSR) = num of successful grasps/num of total grasps, and (2) De-clutter Rate (DR) = num of grasped objects/num of total objects. For each task, we conducted five iterations of testing, with each iteration containing 100 rounds (5 objects per round). A round ends when either all objects are cleared or two consecutive grasp failures occur.

The results reported in Table.1 indicate that our method outperforms all baselines across both settings and tasks in terms of both GSR and DR. The high GSR indicates that our model can predict accurate grasp quality. On the other hand, the high DR signifies that our model infers accurate grasp poses that do not move objects outside of the workspace. Interestingly, our model performs well even though point centers are selected differently at training time (centered on object segments) and test time (selected using FPS), i.e., as described in Section 4.3. This demonstrates that the grasp quality function $\bar{\Gamma}$ output by our method exhibits strong robustness to different point cloud geometries.

5.2 Physical Experiments

To assess our method’s real-world performance, we conduct physical experiments involving two tasks under two camera settings, replicating those in the simulation. We directly transfer the trained model from the simulation to the real-world setting to evaluate the performance gap between them.

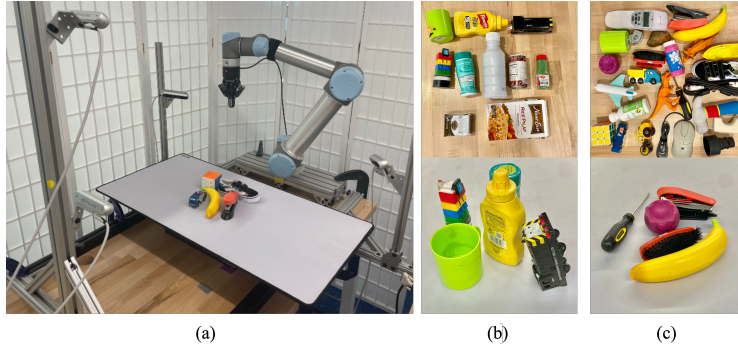


Figure 5. **Real world Experiment Setting.** (a) Robot platform setup. (b) Upper: Packed object set with 10 objects. Bottom: Packed scene (c) Upper: Pile object set with 25 objects. Bottom: Pile scene

Setting	Method	Packed		Pile	
		GSR (%)	DR (%)	GSR (%)	DR (%)
Single-view	VNEdgeGrasp [8]	88.9(96/108)	96.0(96/100)	88.2(97/110)	97.0(97/100)
	OrbitGrasp (Ours)	92.5(98/106)	98.0(98/100)	93.2(97/104)	98.0(98/100)
Multi-view	VNEdgeGrasp [8]	90.1(100/111)	100.0(100/100)	92.1(93/101)	97.0(97/100)
	OrbitGrasp (Ours)	95.2(100/105)	100.0(100/100)	94.3(99/105)	99.0(99/100)

Table 2. We compared the results of OrbitGrasp with VNEdgeGrasp [8] using the same metrics as in the simulation experiments. Our experiment settings for single-view and multi-view are shown in Figure.5. Sometimes, a single trial resulted in grasping two objects simultaneously.

Setup: As shown in Figure.5 (a), a UR5 robot arm is equipped with a Robotiq-85 Gripper. We mount and calibrate 4 RealSense D455 cameras on the table. In the multi-view setting, 3 low-mounted cameras capture the scene for full observation. In the single view setting, we use the top-mounted camera. After obtaining the point cloud, we crop it to the workspace, filter outliers, and calculate the surface normals at each point. We do *not* crop the table from our point clouds. Objects are placed on the table as follows. In the **Packed** setting, we draw 5 objects uniformly at random from the set of 10 objects shown at the top of Figure. 5 (b) and place them in upright orientations with a randomly selected planar position and orientation. In the **Pile** setting, we draw 5 objects uniformly at random from the set of 25 objects shown at the top of Figure. 5 (c) and dump them onto a tabletop out of a box. We conduct 10 rounds of experiments for the **Packed** scene and 4 rounds for the **Pile** scene for each view setting. We configure our method as follows. We use $k = 10$ center points selected using height-thresholded FPS to form the neighborhoods B_1, \dots, B_k . From the orbit of each point, we evenly sample 36 grasp poses and evaluate them based on the grasp quality function from the network. After filtering out unreachable and low-quality poses (i.e. grasp poses with a quality < 0.95), we select the pose with the highest Z value.

Results: We baseline our method against VNEdgeGrasp [8]. The results are shown in Table.2. In the single view **Packed** task, the GSR of our model outperformed VNEdgeGrasp by an average of 3.6% and by 5% in the single view **Pile** task. In the multi-view setting, our model’s GSR outperformed by 5.1% on the **Packed** task and by 2.2% on the **Pile** task. We analyze the failure modes we encountered in Appendix D.

5.3 Ablation Study

In our ablation study, we measure the significance of network equivariance by comparing to PointNet++ [48], a well-known non-equivariant model under a single random camera setting, keeping all settings identical except for the network structure. For fairness, we set up PointNet++ so that it has the same number of parameters as our method. We also measure the influence of different degrees of spherical harmonics, where higher degrees correspond to more basis functions and larger numbers of Fourier coefficients. The results, shown in Table.3, indicate that PointNet++ performs poorly (GSR of 60.5% versus 96.7% for the **Pile** task), presumably due to the lack of equivariance

Model	#Params	Packed		Pile	
		GSR (%)	DR (%)	GSR (%)	DR (%)
PointNet++ [48]	14M	78.1 ± 2.9	78.8 ± 1.9	60.5 ± 1.8	54.1 ± 2.7
OrbitGrasp ($l = 1, m = 1$)	4M	94.2 ± 1.2	96.3 ± 1.3	93.9 ± 0.5	97.0 ± 0.7
OrbitGrasp ($l = 2, m = 2$)	8M	97.4 ± 0.5	98.5 ± 0.6	96.3 ± 1.0	97.6 ± 0.7
OrbitGrasp ($l = 3, m = 2$)	14M	98.3 ± 0.7	98.8 ± 0.6	96.7 ± 1.1	97.9 ± 0.5

Table 3. Comparison results between non-equivariant and equivariant networks with varying degrees of SH.

in $SO(3)$ space. Interestingly, even with spherical harmonic basis functions of degree 1, our network performs well (GSR of 93.9% for the *Pile* task), a result we attribute to the capabilities of our UNet-based EquiFormerV2, which effectively captures both local and global information. As the degree increases, the performance improvement from additional parameters diminishes. Although the performance of ours ($l = 3, m = 2$) is slightly better (GSR of 96.7% for the *Pile* task) than ($l = 2, m = 2$), it requires nearly double the parameters. This trade-off should be considered when computing power is limited. We also analyze the impact of larger neighborhoods B_i and data augmentation on performance in simulation, as well as different training data generation methods (Mask versus FPS) in the real world, as detailed in Appendix E.

6 Conclusion and Limitations

In this paper, we propose *OrbitGrasp*, a grasp detection method that exploits $SE(3)$ -equivariance to achieve state-of-the-art performance. Our model learns a *continuous* grasp function over S^2 for each point in the point cloud. Using a geometric prior, we constrain potential grasp poses around the surface normal direction of each candidate contact point, forming an orbit. By evaluating densely sampled poses along the orbit with the learned grasp function, multiple good grasp poses can be identified. Simulation experiments demonstrate that our model outperforms several strong baselines across different grasping tasks and settings. Physical experiments show high grasp success rates and good generalization across diverse objects. Our work has several limitations. First, inference time is relatively long because PyTorch is not well optimized for the geometric operations used by EquiFormerV2 and because it is necessary to evaluate multiple point neighborhoods, B_1, \dots, B_k . One approach to solving this problem would be to incorporate gauge equivariance [49] and predict directly in the tangent space [50], which would lower the dimensionality of the problem and speed up inference. Another limitation is there is no direct mechanism for constraining the grasp of specific objects or object parts. Future work may address this challenge by incorporating methods for conditioning on language or object crops.

Acknowledgments

This work is supported in part by NSF 1724257, NSF 1724191, NSF 1763878, NSF 1750649, NSF 2107256, NSF 2134178, NSF 2312171, and NASA 80NSSC19K1474. Dian Wang is supported in part by the JPMorgan Chase PhD fellowship. The authors would like to thank Owen Howell and David Klee for their valuable discussions and advice on designing the $SE(3)$ -equivariant network and preparing the paper manuscript.

References

- [1] X. Zhu, D. Wang, O. Biza, G. Su, R. Walters, and R. Platt. Sample efficient grasp learning using equivariant models. *arXiv preprint arXiv:2202.09468*, 2022.
- [2] H.-S. Fang, C. Wang, H. Fang, M. Gou, J. Liu, H. Yan, W. Liu, Y. Xie, and C. Lu. Anygrasp: Robust and efficient grasp perception in spatial and temporal domains. *IEEE Transactions on Robotics*, 2023.
- [3] A. Mousavian, C. Eppner, and D. Fox. 6-dof graspnet: Variational grasp generation for object manipulation. In *Proceedings of the IEEE/CVF international conference on computer vision*, pages 2901–2910, 2019.
- [4] M. Sundermeyer, A. Mousavian, R. Triebel, and D. Fox. Contact-graspnet: Efficient 6-dof grasp generation in cluttered scenes. In *2021 IEEE International Conference on Robotics and Automation (ICRA)*, pages 13438–13444. IEEE, 2021.
- [5] M. Breyer, J. J. Chung, L. Ott, R. Siegwart, and J. Nieto. Volumetric grasping network: Real-time 6 dof grasp detection in clutter. In *Conference on Robot Learning*, pages 1602–1611. PMLR, 2021.
- [6] U. Asif, J. Tang, and S. Harrer. Graspnet: An efficient convolutional neural network for real-time grasp detection for low-powered devices. In *IJCAI*, volume 7, pages 4875–4882, 2018.
- [7] A. Ten Pas, M. Gualtieri, K. Saenko, and R. Platt. Grasp pose detection in point clouds. *The International Journal of Robotics Research*, 36(13-14):1455–1473, 2017.
- [8] H. Huang, D. Wang, X. Zhu, R. Walters, and R. Platt. Edge grasp network: A graph-based $se(3)$ -invariant approach to grasp detection. In *2023 IEEE International Conference on Robotics and Automation (ICRA)*, pages 3882–3888. IEEE, 2023.
- [9] R. Zurbrügg, Y. Liu, F. Engelmann, S. Kumar, M. Hutter, V. Patil, and F. Yu. Icgnet: A unified approach for instance-centric grasping. *arXiv preprint arXiv:2401.09939*, 2024.
- [10] E. B. Dam, M. Koch, and M. Lillholm. *Quaternions, interpolation and animation*, volume 2. Citeseer, 1998.
- [11] Y. Zhou, C. Barnes, J. Lu, J. Yang, and H. Li. On the continuity of rotation representations in neural networks. *CoRR*, abs/1812.07035, 2018. URL <http://arxiv.org/abs/1812.07035>.
- [12] M. Jia, D. Wang, G. Su, D. Klee, X. Zhu, R. Walters, and R. Platt. Seil: Simulation-augmented equivariant imitation learning. In *2023 IEEE International Conference on Robotics and Automation (ICRA)*, pages 1845–1851. IEEE, 2023.
- [13] A. Simeonov, Y. Du, Y.-C. Lin, A. R. Garcia, L. P. Kaelbling, T. Lozano-Pérez, and P. Agrawal. $Se(3)$ -equivariant relational rearrangement with neural descriptor fields. In *Conference on Robot Learning*, pages 835–846. PMLR, 2023.

- [14] A. Simeonov, Y. Du, A. Tagliasacchi, J. B. Tenenbaum, A. Rodriguez, P. Agrawal, and V. Sitzmann. Neural descriptor fields: Se (3)-equivariant object representations for manipulation. In *2022 International Conference on Robotics and Automation (ICRA)*, pages 6394–6400. IEEE, 2022.
- [15] H. H. Nguyen, A. Baisero, D. Klee, D. Wang, R. Platt, and C. Amato. Equivariant reinforcement learning under partial observability. In *Conference on Robot Learning*, pages 3309–3320. PMLR, 2023.
- [16] D. Wang, M. Jia, X. Zhu, R. Walters, and R. Platt. On-robot learning with equivariant models. *arXiv preprint arXiv:2203.04923*, 2022.
- [17] Y.-L. Liao, B. Wood, A. Das, and T. Smidt. Equiformerv2: Improved equivariant transformer for scaling to higher-degree representations. *arXiv preprint arXiv:2306.12059*, 2023.
- [18] Z. Jiang, Y. Zhu, M. Svetlik, K. Fang, and Y. Zhu. Synergies between affordance and geometry: 6-dof grasp detection via implicit representations. *arXiv preprint arXiv:2104.01542*, 2021.
- [19] H.-S. Fang, C. Wang, M. Gou, and C. Lu. Graspnet-1billion: A large-scale benchmark for general object grasping. In *Proceedings of the IEEE/CVF conference on computer vision and pattern recognition*, pages 11444–11453, 2020.
- [20] N. Thomas, T. Smidt, S. Kearnes, L. Yang, L. Li, K. Kohlhoff, and P. Riley. Tensor field networks: Rotation-and translation-equivariant neural networks for 3d point clouds. *arXiv preprint arXiv:1802.08219*, 2018.
- [21] C. Deng, O. Litany, Y. Duan, A. Poulencard, A. Tagliasacchi, and L. J. Guibas. Vector neurons: A general framework for so (3)-equivariant networks. In *Proceedings of the IEEE/CVF International Conference on Computer Vision*, pages 12200–12209, 2021.
- [22] Z. Weng, H. Lu, J. Lundell, and D. Kragic. Capgrasp: An $\mathbb{R}^3 \times \text{SO}(2)$ -Equivariant continuous approach-constrained generative grasp sampler. *IEEE Robotics and Automation Letters*, 9(4): 3641–3647, 2024. doi:10.1109/LRA.2024.3369444.
- [23] S. Jauhri, I. Lunawat, and G. Chalvatzaki. Learning any-view 6dof robotic grasping in cluttered scenes via neural surface rendering. *arXiv preprint arXiv:2306.07392*, 2023.
- [24] D. Wang, R. Walters, X. Zhu, and R. Platt. Equivariant q learning in spatial action spaces. In *Conference on Robot Learning*, pages 1713–1723. PMLR, 2022.
- [25] D. Wang, R. Walters, and R. Platt. $\text{SO}(2)$ -equivariant reinforcement learning. *arXiv preprint arXiv:2203.04439*, 2022.
- [26] T. Cohen and M. Welling. Group equivariant convolutional networks. In *International conference on machine learning*, pages 2990–2999. PMLR, 2016.
- [27] T. S. Cohen and M. Welling. Steerable cnns. *arXiv preprint arXiv:1612.08498*, 2016.
- [28] H. Huang, D. Wang, R. Walters, and R. Platt. Equivariant transporter network. *arXiv preprint arXiv:2202.09400*, 2022.
- [29] A. Zeng, P. Florence, J. Tompson, S. Welker, J. Chien, M. Attarian, T. Armstrong, I. Krasin, D. Duong, V. Sindhwani, et al. Transporter networks: Rearranging the visual world for robotic manipulation. In *Conference on Robot Learning*, pages 726–747. PMLR, 2021.
- [30] H. Ryu, H.-i. Lee, J.-H. Lee, and J. Choi. Equivariant descriptor fields: Se (3)-equivariant energy-based models for end-to-end visual robotic manipulation learning. *arXiv preprint arXiv:2206.08321*, 2022.

- [31] H. Huang, O. Howell, X. Zhu, D. Wang, R. Walters, and R. Platt. Fourier transporter: Bi-equivariant robotic manipulation in 3d. *arXiv preprint arXiv:2401.12046*, 2024.
- [32] B. Eisner, Y. Yang, T. Davchev, M. Vecerik, J. Scholz, and D. Held. Deep se (3)-equivariant geometric reasoning for precise placement tasks. *arXiv preprint arXiv:2404.13478*, 2024.
- [33] C. Gao, Z. Xue, S. Deng, T. Liang, S. Yang, L. Shao, and H. Xu. Riemann: Near real-time se (3)-equivariant robot manipulation without point cloud segmentation. *arXiv preprint arXiv:2403.19460*, 2024.
- [34] H. Liang, X. Ma, S. Li, M. Görner, S. Tang, B. Fang, F. Sun, and J. Zhang. Pointnetgpd: Detecting grasp configurations from point sets. In *2019 International Conference on Robotics and Automation (ICRA)*, pages 3629–3635. IEEE, 2019.
- [35] A. W. Knap and A. W. Knap. *Lie groups beyond an introduction*, volume 140. Springer, 1996.
- [36] Y.-L. Liao and T. Smidt. Equiformer: Equivariant graph attention transformer for 3d atomistic graphs. *arXiv preprint arXiv:2206.11990*, 2022.
- [37] S. Passaro and C. L. Zitnick. Reducing so (3) convolutions to so (2) for efficient equivariant gnns. In *International Conference on Machine Learning*, pages 27420–27438. PMLR, 2023.
- [38] H. Ryu, J. Kim, J. Chang, H. S. Ahn, J. Seo, T. Kim, J. Choi, and R. Horowitz. Diffusion-edfs: Bi-equivariant denoising generative modeling on se (3) for visual robotic manipulation. *arXiv preprint arXiv:2309.02685*, 2023.
- [39] E. Coumans and Y. Bai. Pybullet, a python module for physics simulation for games, robotics and machine learning. 2016.
- [40] B. Calli, A. Singh, A. Walsman, S. Srinivasa, P. Abbeel, and A. M. Dollar. The ycb object and model set: Towards common benchmarks for manipulation research. In *2015 international conference on advanced robotics (ICAR)*, pages 510–517. IEEE, 2015.
- [41] A. Singh, J. Sha, K. S. Narayan, T. Achim, and P. Abbeel. Bigbird: A large-scale 3d database of object instances. In *2014 IEEE international conference on robotics and automation (ICRA)*, pages 509–516. IEEE, 2014.
- [42] A. Kasper, Z. Xue, and R. Dillmann. The kit object models database: An object model database for object recognition, localization and manipulation in service robotics. *The International Journal of Robotics Research*, 31(8):927–934, 2012.
- [43] D. Kappler, J. Bohg, and S. Schaal. Leveraging big data for grasp planning. In *2015 IEEE international conference on robotics and automation (ICRA)*, pages 4304–4311. IEEE, 2015.
- [44] A. Kirillov, E. Mintun, N. Ravi, H. Mao, C. Rolland, L. Gustafson, T. Xiao, S. Whitehead, A. C. Berg, W.-Y. Lo, P. Dollár, and R. Girshick. Segment anything. *arXiv:2304.02643*, 2023.
- [45] I. Loshchilov and F. Hutter. Decoupled weight decay regularization. *arXiv preprint arXiv:1711.05101*, 2017.
- [46] I. Loshchilov and F. Hutter. Sgdr: Stochastic gradient descent with warm restarts. *arXiv preprint arXiv:1608.03983*, 2016.
- [47] G. E. Hinton, N. Srivastava, A. Krizhevsky, I. Sutskever, and R. R. Salakhutdinov. Improving neural networks by preventing co-adaptation of feature detectors. *arXiv preprint arXiv:1207.0580*, 2012.
- [48] C. R. Qi, L. Yi, H. Su, and L. J. Guibas. Pointnet++: Deep hierarchical feature learning on point sets in a metric space. *Advances in neural information processing systems*, 30, 2017.

- [49] M. M. Bronstein, J. Bruna, T. Cohen, and P. Veličković. Geometric deep learning: Grids, groups, graphs, geodesics, and gauges. *arXiv preprint arXiv:2104.13478*, 2021.
- [50] P. De Haan, M. Weiler, T. Cohen, and M. Welling. Gauge equivariant mesh cnns: Anisotropic convolutions on geometric graphs. In *International Conference on Learning Representations*, 2020.

A Mask-Based Sample Generation

To obtain object masks on a point cloud, all RGB-D images are first cropped to focus on the workspace area. The Segment Anything Model [44] is then applied to each RGB image to acquire 2D segmentation masks of all objects. Given the pixel-wise correspondence between the RGB image, masks, and depth map, we can map these 2D masks onto the point cloud using the depth information and transformation matrices. Note that each point \mathbf{p}_i may belong to multiple masks, such as $\mathbf{p}_i \in \mathbf{M}_a$ and $\mathbf{p}_i \in \mathbf{M}_b$, where \mathbf{M}_a and \mathbf{M}_b are different masks. By combining the point clouds and mask information from multiple cameras, a raw mask-centric point cloud representation is reconstructed. After preprocessing and filtering, we finally obtain the refined mask-centric point cloud scene, illustrated in Figure. 6.

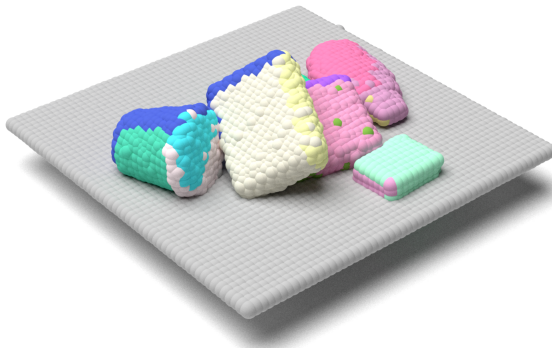


Figure 6. The mask-centric point cloud representation. Each mask is rendered in a distinct color. Points that belong to multiple masks are rendered with only one color.

In our implementation, we use the centers of the individual object masks as center points to construct B_i for generating grasp poses during training data collection. This method provides more even point sampling compared to the FPS-based method, ensuring a more uniform distribution of grasp points. Additionally, it avoids generating many unstable poses on the edges and corners of objects. Although FPS is still used to construct B_i during inference, we found that our model effectively reduces the probability of grasping the edges or corners of objects.

B Model Architecture

The detailed architecture of EquiFormerV2, as mentioned in Section 4.5, is illustrated in Figure. 7. To keep the equivariance property of the network, the features in EquiFormerV2 are based on vector spaces of irreps, and operations such as layer normalization, S^2 activation functions, and learnable functions are designed to be equivariant. Additionally, EquiFormerV2 includes eSCN [37] convolution layers, which consist of a rotation matrix D_{ij} and an $SO(2)$ linear layer. This approach reduces the computational complexity of $SO(3)$ tensor products, thereby enabling efficient interaction of information across both degrees and channels and allowing EquiFormer to scale effectively to a higher degree L .

Compared to the original structure, we have made several key modifications. The original $SO(3)$ embedding has been replaced with a single equivariant linear layer that takes the point normal directions as input directly. This embedding is then used in subsequent blocks. After the first equivariant graph attention block, we apply FPS to downsample the point cloud. For each downsampled point, we use KNN to find its neighbors and build edges between them. During upsampling, we reverse these edges from each downsampling block by swapping the source and destination of these edges. This allows us to gradually transfer information from the downsampled points to the points in the upsampling blocks. The theoretical foundation and mathematical proof of EquiFormerV2 can be found in [17, 36, 37].

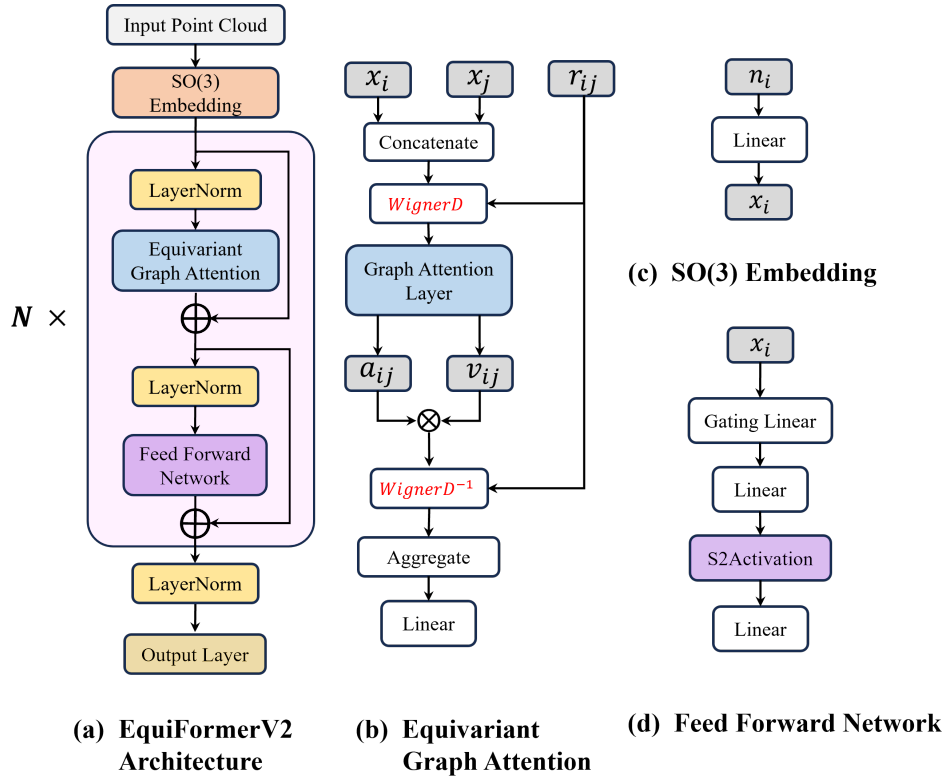


Figure 7. **Overview of the EquiFormerV2 architecture.** (a) shows the overall structure of EquiFormerV2, while (b), (c), and (d) illustrate the submodules of (a). Multiple EquiFormerV2 blocks, incorporating FPS and KNN layers for connectivity, are stacked to form our UNet-style architecture.

C Simulation Additional Details

We provide several figures (Figure. 8, 9) to give more information about the simulation environment and the grasp pose evaluation process.

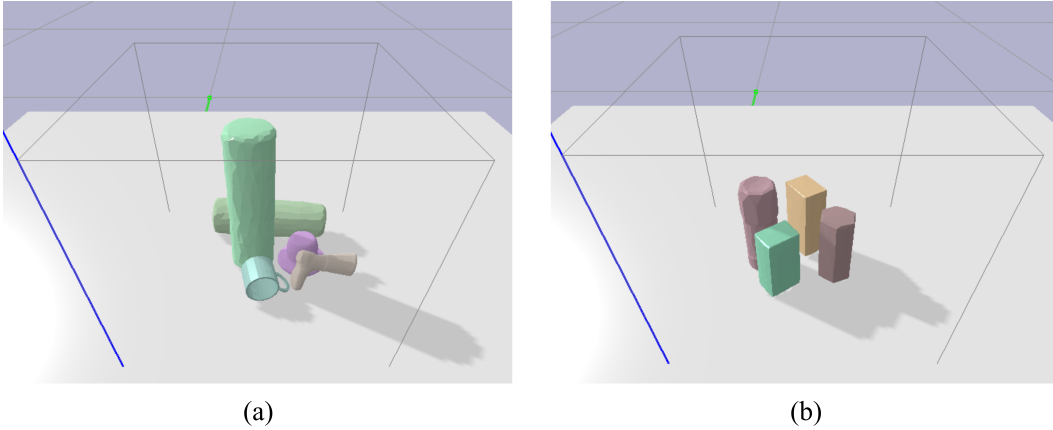


Figure 8. (a) and (b) illustrate examples of “pile” and “packed” scenes, respectively.

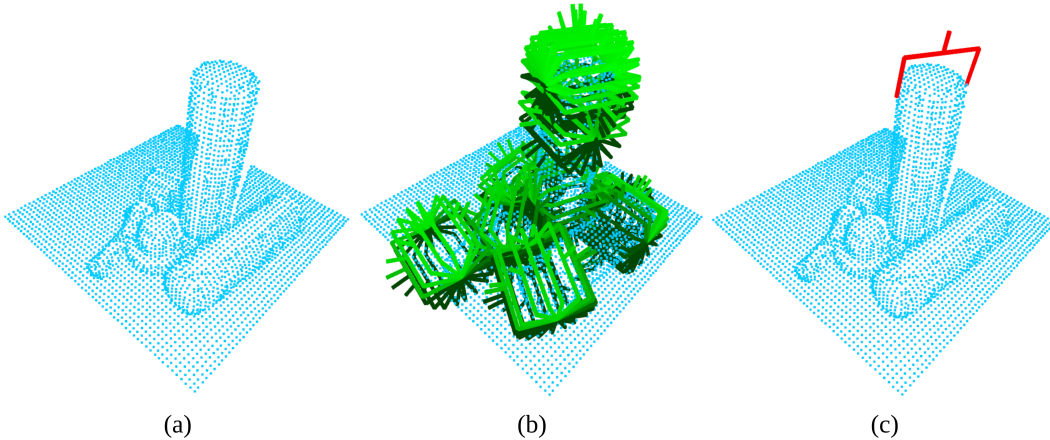


Figure 9. (a) The downsampled point cloud. (b) We show sampled grasp poses at the points with the highest grasp quality scores in each of the 10 \mathcal{B}_i . A more intense green color indicates higher quality. For simplicity, only 18 of the 36 sampled poses per point are displayed. (c) The best grasp poses among all $\mathcal{B}_{1,\dots,n}$.

D Physical Experiments Additional Details

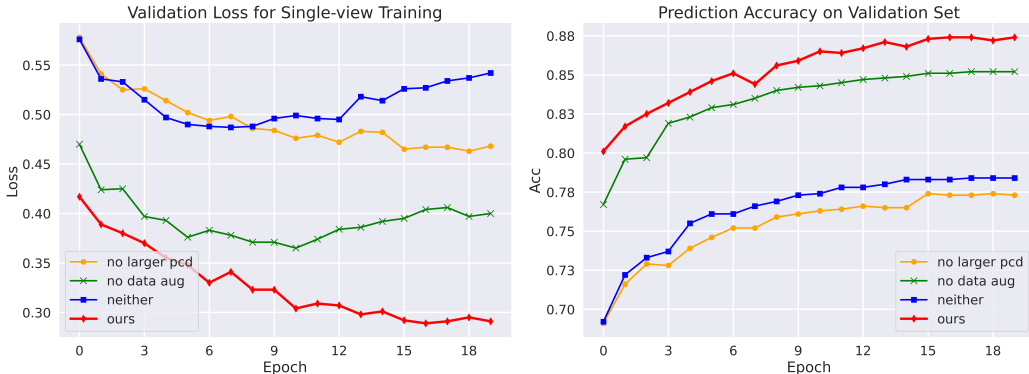
Implementation Details. Although our design initially selects the grasp pose with the highest Z value after filtering, we observed that this highest Z value can sometimes be unstable on the physical robot, unlike in simulations. Therefore, because our method generates a series of grasping poses for each point, we also consider poses within a 3cm range below the highest grasp pose. If a pose within this range has the highest grasp quality (i.e., it is at least better than the highest pose), we select it instead. This approach effectively reduces failures caused by weak grasping and mitigates the sim-to-real gap.

Failure Mode Analysis. In the single-view setting, we observe that the GSR of our method for the *Packed* scene is lower than that for the *Pile* scene, which is inconsistent with the simulation results. The primary failure mode (5/8) involves a white bottle that blends with the table mat color.

This blending results in inaccurate depth and point cloud shape estimation by the camera, preventing the gripper from being inserted deeply enough to provide sufficient friction. For the *Pile* task, the primary reason for failure is the thickness of the objects, where thin objects cause their point cloud to merge with that of the table, distorting the shape of objects. This distortion leads to inaccurate normal estimation and unreasonable poses generated by our model. Additionally, the smooth surface and specific shape of some objects lead to insufficient friction, causing objects like stones to slip out of the gripper’s hand. In the multi-view setting, the overall tendency of failure is similar to the single-view setting. While the point clouds from different perspectives help mitigate the distortion problem, introducing more cameras also introduces calibration errors between them. These errors, in turn, transfer to noises that appear in the point cloud.

E Full Ablation Results

Larger Point Cloud as Input and Data Augmentation. As mentioned in Section 4.3, we emphasize the importance of using a larger point cloud $B_i = \mathcal{N}(c_i, m)$ instead of just the local point cloud $\mathcal{B}_i = \mathcal{B}(c_i, r_l)$ is crucial for eliminating boundary effects by providing more context. To evaluate this, we compare the performance of these two input formats. Besides, despite our network being SE(3)-equivariant, overfitting remains a concern. Therefore, we also assess the impact of data augmentation by comparing results with and without random rotations of the point cloud in SE(3) space before each SGD step. The results, shown in Figure 10, indicate that using the larger point cloud as input significantly improves performance, as evidenced by lower loss and higher prediction accuracy. Moreover, we also find that without data augmentation, validation loss increases in the later stages of training, regardless of other strategies used. These findings underscore the necessity of larger point clouds for providing context and the importance of data augmentation.



(a). The validation loss trends.

(b). The predicted accuracy of all validation poses.

Figure 10. The ablation study results of larger point cloud as input and data augmentation.

Performance Comparison Between Mask-Based and FPS-Based Training Data. We compared the effects of mask-based versus FPS-based training data. Although both methods perform similarly in simulations, differences appear in real-world experiments. As shown in Figure 11, with the same input, the grasp quality distribution from the mask-based trained network is more uniform and centered around the object’s center of mass (e.g., the banana, hammer, and shoe). This indicates that the mask-based trained network can evaluate a wide range of grasp poses more effectively. In contrast, the FPS-based trained network tends to produce grasps biased towards the object’s edges or specific small regions. These edge-focused poses are relatively unstable than those around the center of mass. We interpret this as a result of FPS-based training lacking object-centric awareness, which causes the network to focus on specific areas, and consequently, it struggles to effectively assess grasps at other positions. Mask-based training data, however, incorporates object-centric information. This enables the network to evaluate grasp poses across the entire object. Therefore,

even when FPS is used for input during inference, the network maintains enough robustness to handle unseen geometric information.

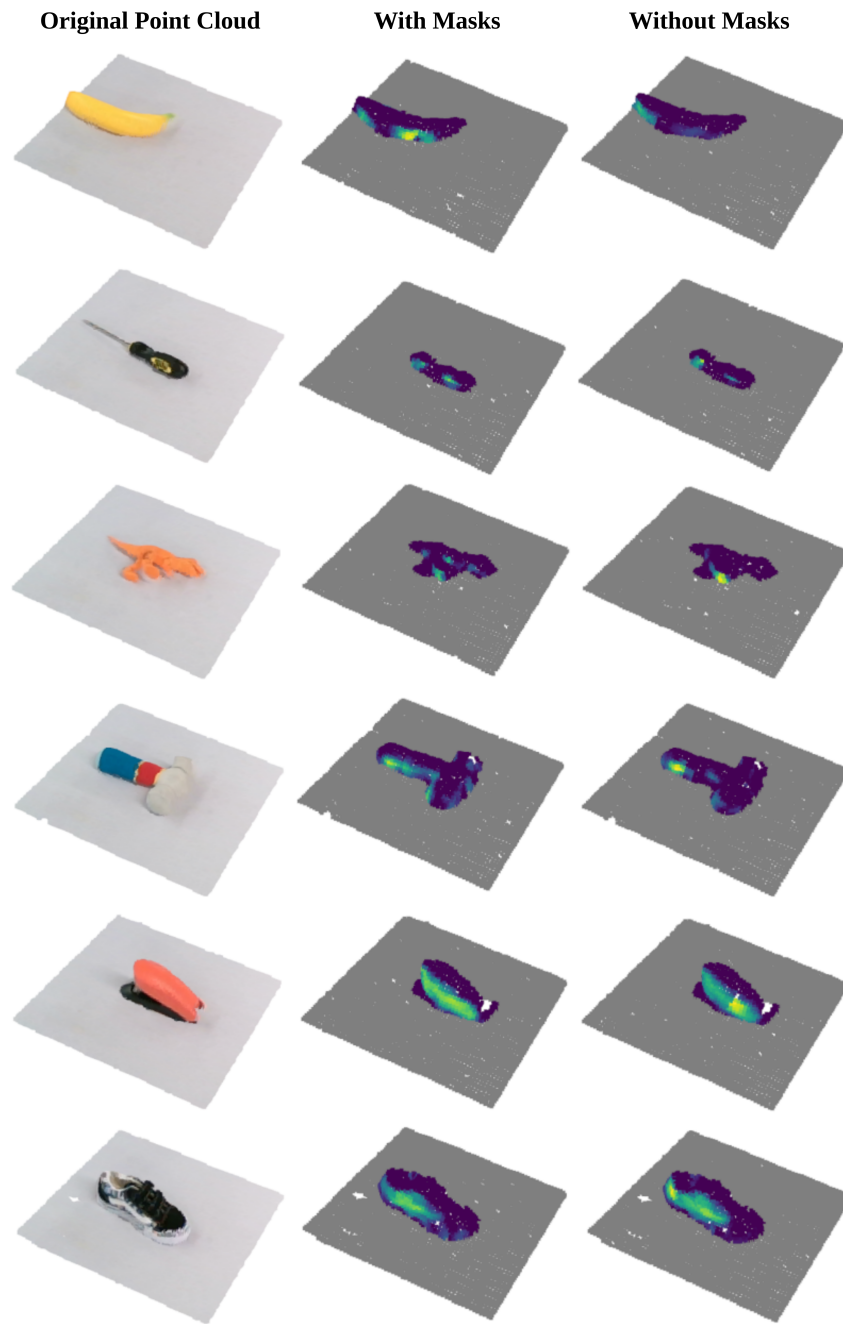


Figure 11. **Grasp quality distribution for different training data generation strategies.** The highest grasp quality of all sampled poses at each point represents that point's quality. The left column displays the original point cloud. The middle column shows predictions from the network trained with mask-based data. The right column shows predictions from the network trained with FPS-based data.